remote sensing

MDPI

Article

Seismic Remote Sensing of Super Typhoon Lupit (2009) with Seismological Array Observation in NE China

Jianmin Lin [1], Yating Wang [1], Weitao Wang [2], Xiaofeng Li [1,3,*], Sunke Fang [1], Chao Chen [1] and Hong Zheng [1]

1 Marine Acoustics and Remote Sensing Laboratory, Zhejiang Ocean University, Zhoushan 316021, China; jmlin007@zjou.edu.cn (J.L.); adelinewyt1@gmail.com (Y.W.); fangsunke@outlook.com (S.F.); chenchao@zjou.edu.cn (C.C.); seahzheng@msn.com (H.Z.)

2 Key Laboratory of Seismic Observation and Geophysical Imaging, Institute of Geophysics, China Earthquake Administration, Beijing 100081, China; wangwt@cea-igp.ac.cn

3 Global Science and Technology, National Oceanic and Atmospheric Administration (NOAA)-National Environmental Satellite, Data, and Information Service (NESDIS), College Park, MD 20740, USA

* Correspondence: xiaofeng.li@noaa.gov; Tel.: +1-301-683-3144

Received: 26 December 2017; Accepted: 1 February 2018; Published: 3 February 2018

Abstract: The *p*-wave double-frequency (DF) microseisms generated by super typhoon Lupit (14–26 October 2009) over the western Pacific Ocean were detected by an on-land seismological array deployed in Northeastern China. We applied a frequency-domain beamforming method to investigate their source regions. Comparing with the best-track data and satellite observations, the located source regions of the *p*-wave DF microseisms, which corresponded to the strongest ocean wave–wave interactions, were found to be comparable to the typhoon centers in the microseismic frequency band of ~0.18–0.21 Hz. The *p*-wave DF microseisms were probably excited by the nonlinear interaction of ocean waves generated by the typhoon at different times, in good agreement with the *Longuet–Higgins* theory for the generation of DF microseisms. The localization deviation, which was ~120 km for typhoon Lupit in this study, might depend on the speed and direction of typhoon movement, the geometry of the seismological array, and the heterogeneity of the solid Earth structure. The *p*-wave DF microseisms generated in coastal source regions were also observed in the beamformer outputs, but with relatively lower dominant frequency band of ~0.14–0.16 Hz. These observations show that the *p*-wave DF microseisms generated near typhoon centers could be used as a seismic remote sensing proxy to locate and track typhoons over the oceans from under water in a near-real-time and continuous manner.

Keywords: microseisms; typhoon; remote sensing; seismological array; ocean wave

1. Introduction

Typhoons usually induce tremendous damage to society, but are still difficult to monitor in real time because of the lack of in situ observations under such extreme weather conditions during the typhoon's passage. Typhoons are normally observed by satellites from space, focusing mainly on the phenomena above the sea surface. A new way of ocean storm monitoring based on acoustic and seismic records of the typhoon-generated noise has emerged recently [1–8], which could estimate the wind speed of typhoons or remotely sense typhoon movement from underneath the typhoon or even from the solid Earth beneath the water. This interdisciplinary approach, spanning ocean acoustics, marine geophysics and physical oceanography, focuses on the generation and propagation of the acoustic and seismic waves generated by typhoons. It is expected to provide an effective complement

to traditional methods of typhoon monitoring, offering the possibility of near-real-time and continuous tracking and intensity inversion.

In recent years, underwater ambient sound beneath typhoons have been investigated and used to estimate the wind speed. Wilson and Makris [2,3] first developed underwater acoustic sensing techniques based on theoretical and empirical evidence. They carried out measurements of 10–50 Hz sound beneath Hurricane Gert in 1999 with a single hydrophone at 800 m depth, and suggested the sound at this frequency band was not affected by bubble attenuation and could be used to monitor the wind speed and quantify the destructive power of typhoons. Zhao et al. [9] measured the underwater ambient sound levels at a frequency band of 40 Hz–50 kHz beneath three different typhoons using hydrophones onboard Lagrangian floats from 1 to 50 m depth, and analyzed the complex relationship between the sound level and the wind speed. However, the highlights of these underwater ambient sound studies were almost focused on the frequency band of several tens Hz and above, and the low-frequency (e.g., <1 Hz) noise generated by the pressure fluctuations due to ocean waves were often filtered out and removed.

Typhoons generate large ocean waves at the sea surface, and some of the energy can propagate to the sea floor and be transferred into seismic waves propagating in the solid Earth as "microseisms" (~0.05–0.5 Hz) [1,7,10,11]. The microseisms can propagate as both surface waves and compressional (*P*) waves, which could even be detected by the seismometers located thousands of kilometers away from the source regions [1,12–15]. In the frequency domain, the microseisms can be divided into two distinct bands due to different generation mechanisms: single-frequency (SF, from about 0.05 to 0.12 Hz) and double-frequency (DF, from about 0.12 to 0.4 Hz) microseisms.

SF microseisms are generated through direct interaction of ocean waves with the shallow seafloor or the shore [16], thus typically having a dominant frequency band corresponding to the ocean-wave frequencies. Because the pressure perturbation induced by ocean waves attenuates exponentially with water depth with an e-folding constant equal to the wavenumber, source regions of SF microseisms are basically located on coastal shallow water areas [17–19]. On the other hand, DF microseisms are thought to be generated by the depth-independent pressure fluctuation on the seafloor induced by nonlinear interactions of ocean waves, which travel in nearly opposite directions with nearly the same period, resulting in their frequencies mainly distributed at twice the ocean-wave frequencies [10]. According to the *Longuet–Higgins* theory, DF microseisms might be generated (1) near the center of a moving storm; or (2) when reflected ocean waves by coastlines interfere with following incident ocean waves; or (3) when ocean waves from two distinct storms cross and interfere [20].

The DF microseisms are traditionally observed to propagate primarily as surface waves (both Rayleigh- and Love-type) originating from near-coastal shallow-water source areas [21–27]. However, with the development of seismological array techniques and array deployment, the *p*-wave DF microseisms generated under storms in deep oceans have been identified [1,14,15,28–30]. Interestingly, the *p*-wave microseism source areas are found to be comparable to the storm position [15], which might provide a new approach of seismic/acoustic remote sensing of ocean storms using on-land seismometers or ocean-bottom seismometers (OBSs).

Although the microseisms induced by typhoons have been measured and tried to track typhoons historically early in 1940s [31,32], the link between ocean storms and their generated ambient noise including microseisms has recently become a frontier topic in the sphere of seismology and ocean acoustics [9,11,33,34]. Recent examples of these types of studies include analysis on both surface and body wave microseisms generated by the 2005 Hurricane Katrina in the Gulf of Mexico using 150 Southern California stations [1]; tracking of western Pacific typhoons in 2006 using seismic records from OBSs and on-land stations [4]; seismological observations of ocean storms in the South China and East China Sea [6]; investigations of the microseisms induced by the Superstorm Sandy in 2012 as it approached the US east coast using the Earthscope Transportable Array (TA) stations [7]; investigation of the DF microseisms generated by the 2013 tropical cyclone Dumile on the seafloor with a large-scale network of 57 broadband OBSs in the southwestern Indian Ocean [8]. The results show that the

microseisms could be considered as a good proxy for future monitoring and tracking of major storms over the oceans.

This approach of seismic/acoustic remote sensing of ocean storms could be nearly real-time. Ocean waves induced by typhoons propagate in deep water at velocities $c \approx \sqrt{g\lambda/2\pi}$, where g is the gravitational acceleration at the Earth's surface and λ is the wavelength determined by the Airy linear wave theory approximation as $\lambda = gT^2/2\pi$, where T is the wave period. For example, the velocity c and wavelength λ of 10 s waves are about 16 m/s and 160 m, respectively. While seismic waves propagate in solid Earth at much greater velocities (~3.5 km/s for Rayleigh waves and ~6.5–11 km/s for *p* waves). Therefore, seismometers are expected to sense the microseisms nearly at the time of their generation, and reflect immediately the progress of a typhoon and the corresponding ocean wave field [13]. Furthermore, because of the continuity of the seismometer records, the results of this remote sensing approach could also be continuous in time domain.

In this paper, we investigated the *p*-wave DF microseisms generated by super typhoon Lupit (2009) over the western Pacific Ocean using frequency-domain beamforming of on-land seismological array data recorded in Northeastern (NE) China (Figure 1). The results indicate that the *p*-wave DF microseisms generated by nonlinear interactions of ocean waves under typhoons over the deep ocean could be observed by on-land seismometers, which were deployed thousands of kilometers distant from the track line of the typhoon. The source areas of the *p*-wave DF microseisms mainly in ~0.18–0.21 Hz located by the beamforming method are comparable to the typhoon centers, demonstrating that this approach allows for locating and tracking typhoons with good accuracy.

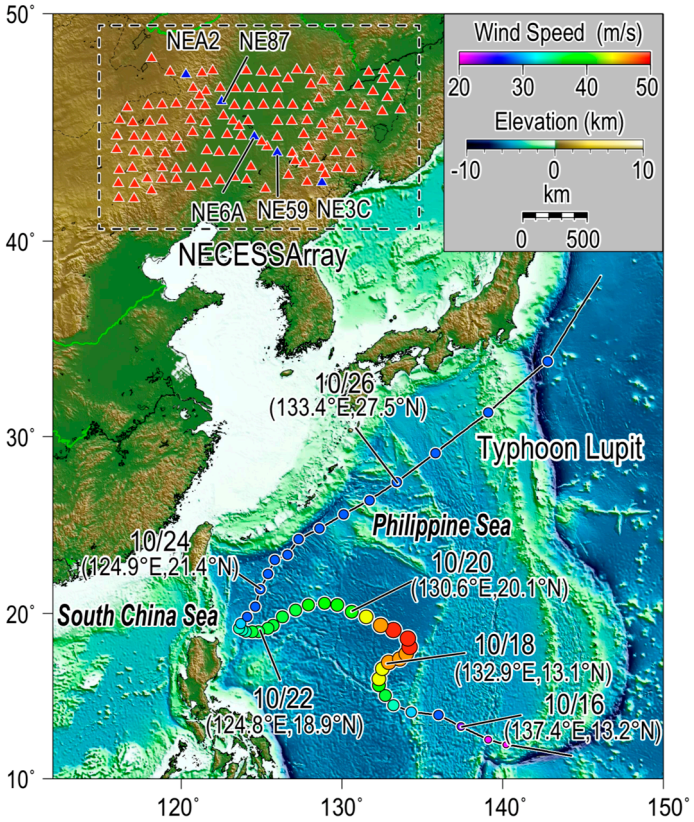

Figure 1. Locations of the 129 NECESSArray stations and the best track of typhoon Lupit in the Philippine Sea with shaded relief bathymetry. The best-track data are from the Japan Meteorological Agency (http://www.jma.go.jp/jma/jma-eng/jma-center/rsmc-hp-pub-eg/trackarchives.html), and are indicated by color-coded round circles spaced in 6-h time intervals, with circle size proportional to wind speed. The seismic stations are represented by red and blue triangles, with the blue ones chosen randomly to display the recording waveforms, as shown in Figure 2.

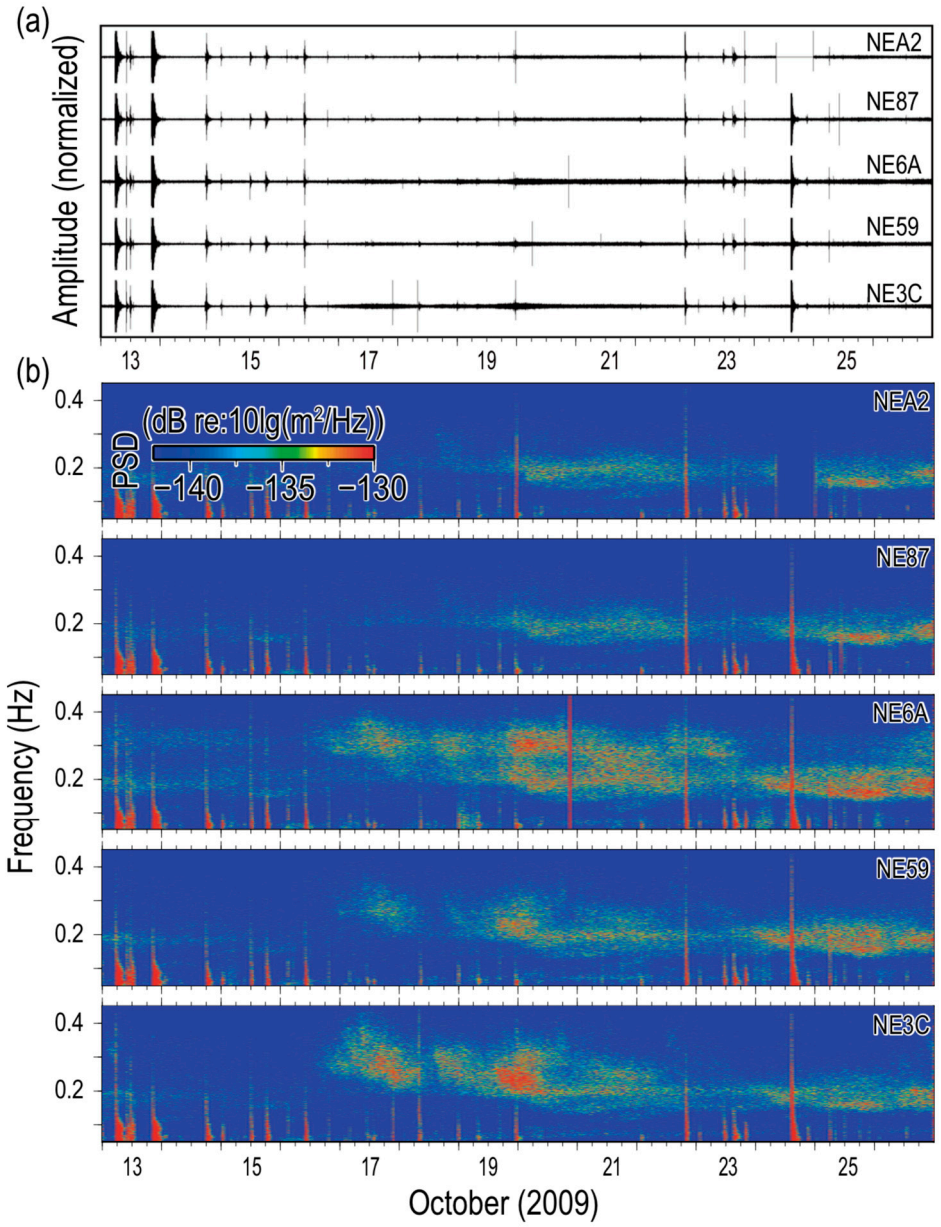

Figure 2. (**a**) Seismic waveforms and (**b**) temporal frequency spectrograms of the microseisms generated during the life span of typhoon Lupit at the stations NEA2, NE87, NE6A, NE3C and NE59 of NECESSArray, labeled by blue triangles in Figure 1. The unit (dB) corresponds to $10 \cdot log_{10}(\mathrm{m}^2/\mathrm{Hz})$.

2. Data

Every year nearly 1/3 of the tropical cyclones all over the world take place over the western Pacific Ocean, making it an ideal place to study tropical cyclones and related topics. This study analyzes the super typhoon Lupit formed on 14 October 2009 and dissipated on 26 October 2009 over the western Pacific Ocean, with category 5 on the Saffir-Simpson scale (Figure 1). According to the best-track data of the Regional Specialized Meteorological Center (RSMC, http://www.jma.go.jp/jma/jma-eng/jma-center/rsmc-hp-pub-eg/RSMC_HP.htm), the track of Lupit is widely distributed over the deep western Pacific Ocean, providing an ideal scenario for the study on the *p*-wave DF microseisms generated by the typhoon under different circumstances. Lupit strengthened into a Category 1 typhoon on 15 October over the open deep Philippine Sea and intensified into Super Typhoon classification with 10-min maximum sustained wind speed up to about 50 m/s and the lowest atmospheric pressure

925 hPa on 18 October. On 23 October, Lupit turned abruptly to the northeast after moving west toward Luzon Island continuously for several days. Finally, Lupit faded out near the Nankai Trough off southeast Japan on 26 October. The entire complicated course with variable moving directions and speed of the typhoon center provides an opportunity for comparison of *p*-wave DF microseisms generated under different conditions.

Continuous seismic waveform data recorded at the NorthEast China Extended SeiSmic Array (NECESSArray, Figure 1), which consisted of 129 seismic stations located in NE China, were obtained from the IRIS Data Management Center (www.iris.edu) and analyzed. The array covers the Greater Hinggan Mountains, the Northeast plain and the Changbai Mountains of China with interstation distance ranging from about 34 to 1510 km. The data was downloaded according to the investigation periods corresponding with the life span of typhoon Lupit.

In order to check if the microseisms generated by the typhoon over the western Pacific Ocean could be detected by single stations of NECESSArray, the temporal frequency spectrogram was applied. First, the original seismic waveform data was preprocessed with the following steps: (1) demeaning and detrending; (2) removal of instrument response; (3) resampling to one point per second; and (4) filtering with a band-pass filter of 0.05–0.45 Hz. Second, the temporal frequency spectrogram was calculated based on the preprocessed data using the Fourier transform with a moving time-window length of 2048 points shifted in steps of 1800 points (i.e., half an hour). For example, Figure 2 shows the waveforms and corresponding temporal frequency spectrograms during the time period of typhoon Lupit at five stations of NECESSArray, which were indicated with blue triangles in Figure 1. The temporal frequency spectrograms detect effectively both the strong DF and some weak SF microseisms generated by Lupit, with little contamination from occasional transient events, such as earthquakes, instrumental irregularities and non-stationary noises, shown as short pulses in the spectra. The recorded microseisms at different stations showed similar temporal evolution pattern during the course of Lupit (Figure 2), and the high spatial coherency between the microseisms initiated the idea to investigate the microseism source with beamforming method [15,35].

The Moderate Resolution Imaging Spectroradiometer (MODIS) data are provided by the National Aeronautics and Space Administration (NASA, https://modis.gsfc.nasa.gov). MODIS is an imaging instrument aboard the Terra and Aqua satellites in NASA's Earth Observing System. It is able to image the same area at different times of the day and cover the entire Earth's surface every one or two days. The MODIS images during the lifespan of typhoon Lupit in all 36 spectral bands including visible, near-infrared, short-wave infrared and thermal infrared bands were obtained. According to the color and texture features of the true color MODIS images created from MODIS Level 1B image and geolocation data, the nephogram and the locations of the typhoon center were distinguished visually and next utilized to compare with the location results by the seismic remote sensing method in this paper.

3. Methods

Seismological array analysis can be used to determine directional information of seismic signals and locate the sources [35]. Since the teleseismic *p*-wave microseisms arrived at the array nearly vertically, the vertical component would record stronger *p*-wave microseismic signals than the horizontal components [1] and was thus used. In order to obtain high resolution in the frequency domain, frequency-domain beamforming method was applied in this study to locate the source areas of the *p*-wave DF microseisms generated by the typhoon and thus further to track the typhoon's movement. The approach is summarized as following [1,26]:

First, the seismic data with 1 Hz sample frequency at each station is split into small segments of 10 min each. The occasional large-amplitude transient events such as earthquakes, instrumental irregularities, and non-stationary noises are removed by truncating the signal amplitude above one standard deviation for each small segment. The segments are then Fourier transformed into spectra, and the amplitude of each frequency is set to 1.0 to keep the phases only. This has similarities with

the time domain normalizing and frequency domain spectrum whitening [36]. This step of amplitude normalization would help remove undesirable signals induced by local site amplification effects and diminish the affection from local noises [14]. Then the cross-spectral density matrix (CSDM) C is constructed at frequency ω by

$$C_{ij,t}(\omega) = \langle F_{i,t}(\omega) F^{\dagger}_{j,t}(\omega) \rangle, \quad (1)$$

where $F(\omega)$ denotes a complex-valued vector from the Fourier transform of the seismograms at a station, † represents the Hermitian transpose operation, and the bracket $\langle\ \rangle$ refers to an ensemble averaging that is performed on successive 10-min windows; t refers to the time of the Fourier transform. The *i*th row and *j*th column of the CSDM C contains the phase delay between stations i and j at frequency ω. In time domain, the right-hand side of Equation (1) corresponds to the cross correlation between the two stations i and j. The beamforming can then be done using the matrix $C(\omega)$.

The object ocean region, which is expected to cover the source areas of the *p*-wave DF microseisms generated by typhoons, is gridded into m × n grids with spatial resolution of 0.1°. Then the array steering vector to each grid (i.e., point source) over the object ocean region, normalized by the number of stations, is given by

$$P(\omega, lat, lon) = \exp(i\omega t_{lat,lon}) / \sqrt{N}, \quad (2)$$

where $t_{lat,lon}$ denotes the travel-time estimates from a grid point to array stations, using a global *p*-wave travel-time model [37]. The beamforming for each segment and each frequency ω is then given by

$$B(\omega, lat, lon) = P^{\dagger}(\omega, lat, lon) C(\omega) P(\omega, lat, lon), \quad (3)$$

where $P^{\dagger}$ denotes the conjugate transpose of the steering vector P.

4. Results and Discussions

4.1. Beamformer Output

The source regions of the *p*-wave DF microseisms generated by typhoon Lupit were successfully revealed and located via frequency-domain beamforming method with the continuous seismic records at the NECESSArray. For example, Figure 3 shows the source locations of the *p*-wave DF microseisms generated by Lupit on the dominant frequency band of 0.18–0.21 Hz (i.e., frequencies with the highest power) at different time points according to the beamformer outputs using the NECESSArray data. A complete animation is available in the electronic supplement.

Compared with the track of typhoon Lupit, which is indicated by solid circles spaced in 6-h time intervals with the white one representing the current location of typhoon center according to the best-track data of RSMC, the source region of the *p*-wave DF microseisms is mainly located behind the current typhoon center, as also observed by Zhang et al. [15]. The *p*-wave DF microseisms might be excited by the nonlinear interaction of the ocean waves propagating at nearly opposite directions with nearly the same periods, which were induced by Lupit at different times [19,20]. The results indicate that the trace of the *p*-wave DF microseism source locations could be a good proxy for the tracking and monitoring of typhoons over the oceans.

4.2. Localization Deviation

However, there are still considerable localization deviations, which are measured by the distances between the localized *p*-wave DF microseism source regions corresponding with the peak amplitudes of the beamformer outputs and the typhoon center locations provided by the best-track data of RSMC. For example, the root-mean-square (RMS) error of the localization results for typhoon Lupit during 06:00 UTC, 19 October to 06:00 UTC, 25 October is about 124.2 km, which is comparable with the track forecast errors using numerical models [38].

The identified *p*-wave DF microseism source locations are also compared with the locations of the typhoon center observed by satellites. Figure 4 shows the observed typhoon eyes during the movement

of Lupit by MODIS-TERRA and MODIS-AQUA at 02:05 UTC, 19 October, 05:05 UTC, 21 October, 04:50 UTC, 23 October, and 02:25 UTC, 24 October. The cloud with high reflectance can be clearly seen on visible band, and the typhoon eyes can be identified using visual interpretation method and labeled with green triangles in the figure. We found that the localized *p*-wave DF microseism source locations, which are marked with red circles in Figure 4, track the typhoon centers measured from MODIS imagery well. Furthermore, Table 1 shows the quantitative comparison between the locations of the typhoon center from satellite observation and the typhoon-generated *p*-wave DF microseism source locations, with mean localization deviation equal to ~103.22 km.

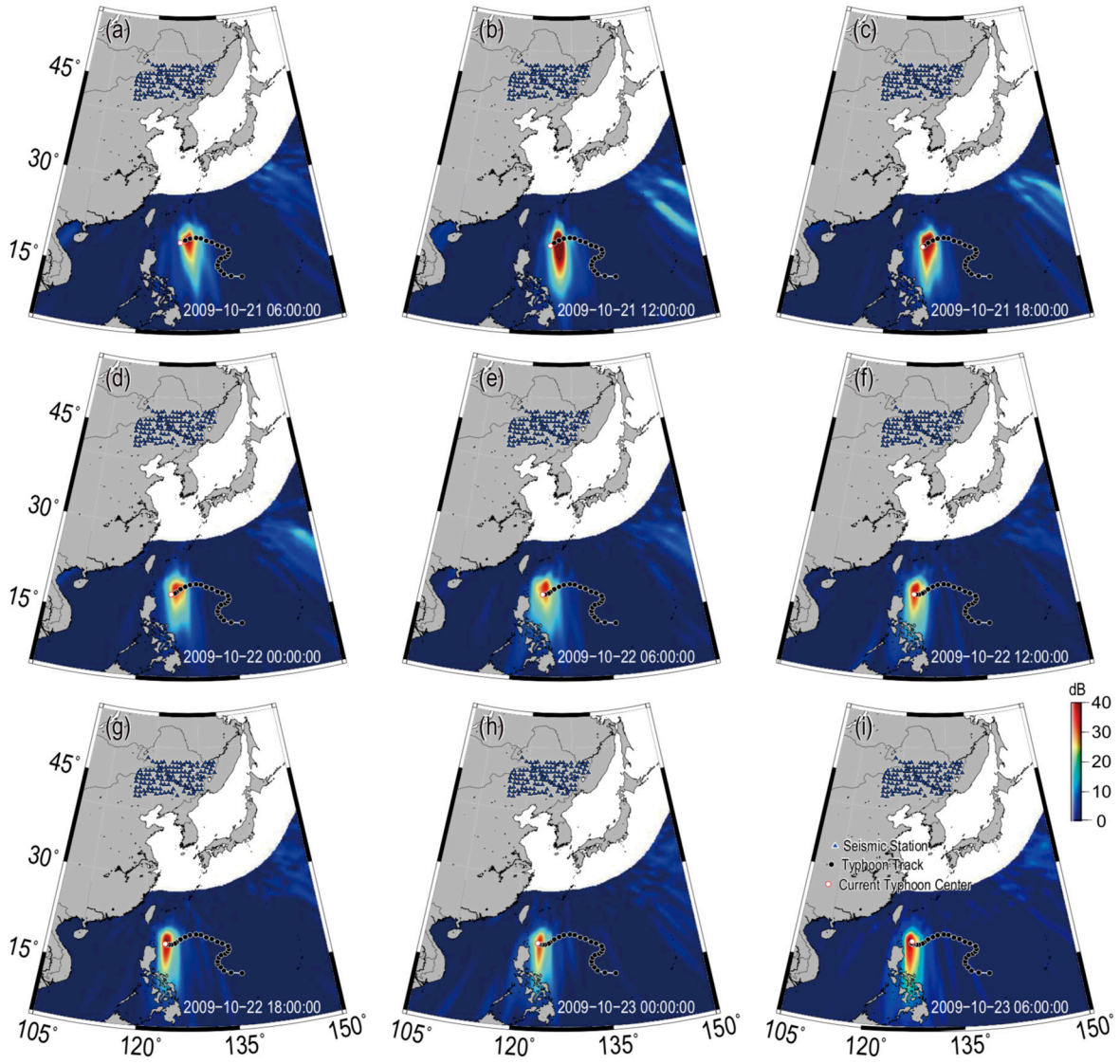

Figure 3. Source locations of Lupit-generated *p*-wave DF microseisms in the form of beamformer outputs using the NECESSArray data at different times: (**a**) 06:00 UTC, 21 October; (**b**) 12:00 UTC, 21 October; (**c**) 18:00 UTC, 21 October; (**d**) 00:00 UTC, 22 October; (**e**) 06:00 UTC, 22 October; (**f**) 12:00 UTC, 22 October; (**g**) 18:00 UTC, 22 October; (**h**) 00:00 UTC, 23 October; and (**i**) 06:00 UTC, 23 October. The beams were calculated and stacked over the frequency band of 0.18–0.21 Hz. The solid circles indicate the track of Lupit with the white one representing the current location of the typhoon center according to the best-track data of the Regional Specialized Meteorological Center (RSMC). A full animation is available in the electronic supplement.

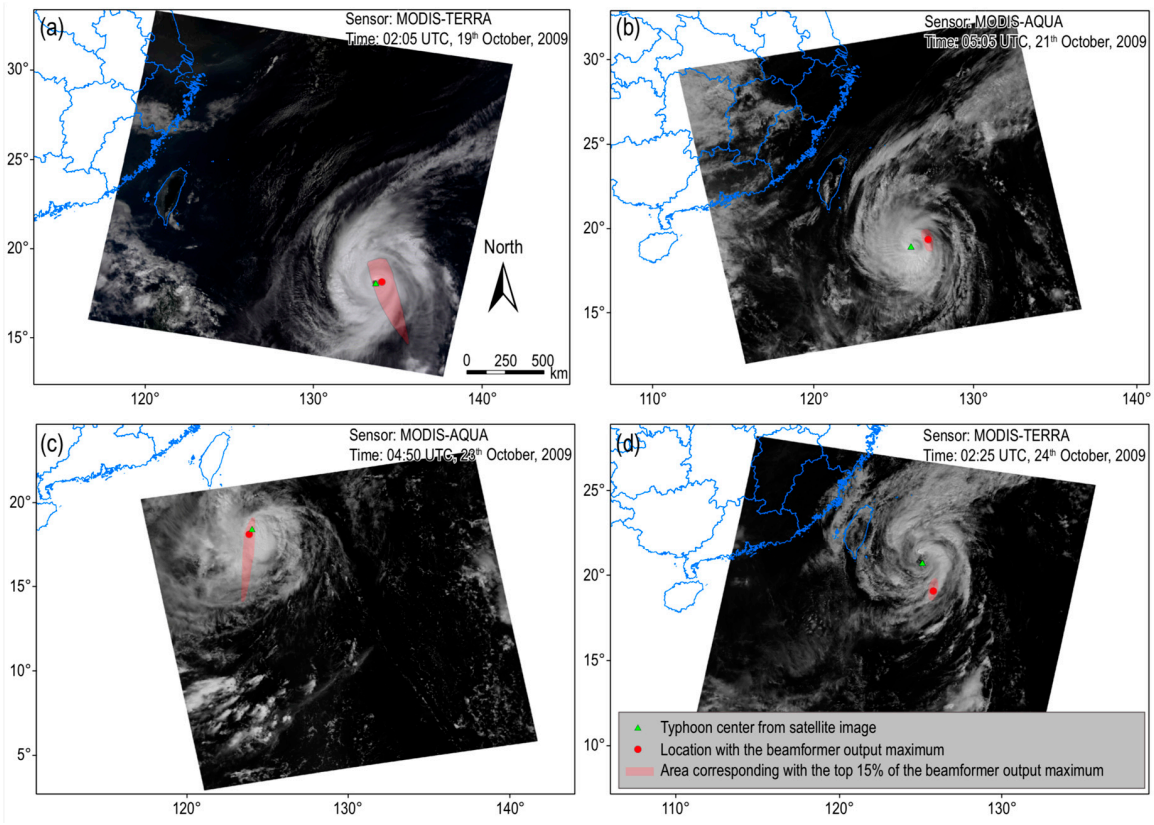

Figure 4. Comparison between the typhoon center locations (green triangles) observed by satellites and the *p*-wave DF microseism source locations calculated according to the beamformer outputs using data at the NECESSArray at different times: (**a**) 02:05 UTC, 19 October; (**b**) 05:05 UTC, 21 October; (**c**) 04:50 UTC, 23 October; and (**d**) 02:25 UTC, 24 October. The base map is true color composites of MODIS images, which rank band composites in order: red band (band 1: 620–670 nm), green band (band 2: 545–565 nm) and blue band (band 3: 459–479 nm).

Table 1. Comparison between the typhoon centers from satellite observation and the typhoon-generated *p*-wave DF microseism source locations.

Acquisition Date and Time (UTC)	Typhoon Eye Location	Satellite	*p*-wave DF Microseism Source Location	Localization Deviation (km)
19 October 2009, 02:05	18.70° N, 133.86° E	TERRA	18.75° N, 134.25° E	41.54
21 October 2009, 05:05	19.65° N, 126.25° E	AQUA	20.05° N, 127.35° E	123.93
23 October 2009, 04:50	19.41° N, 123.72° E	AQUA	19.05° N, 123.55° E	43.42
24 October 2009, 02:25	21.67° N, 125.26° E	TERRA	19.95° N, 125.95° E	203.98

4.3. Causes of Localization Deviations

The localization deviations could arise due to several factors. Besides the intrinsic errors in the beamforming method caused by the heterogeneity of the solid Earth structure and errors due to the large spatial coverage (~300–400 km) of the typhoon center, the typhoon moving speed could be one of the main factors. For the sake of illustration, a typhoon moving northward in the Northern hemisphere was considered (Figure 5a,b). The winds rotate counter-clockwise (CCW) around the typhoon eye, and the highest wind speeds occur in the NE quadrant near the radius-to-maximum-wind, generating the strongest ocean waves propagating mainly in the NW direction [39,40]. When the typhoon is moving slower than the ocean waves propagate, such dominant ocean waves induced at an earlier time t1 would propagate as young swells and interfere with the wind sea around the current

typhoon center at a later time t2. The interactions between the forward and backward ocean waves, as a significant source of the DF microseisms, are mostly located closely behind the typhoon center (Figure 5a). But when the typhoon is moving faster than the ocean waves propagate, the field of such wave-wave interaction would be located more distant behind the typhoon center as shown in Figure 5b. For example, the localized *p*-wave DF microseism source regions during 06:00 UTC, 21 October to 00:00 UTC, 22 October were relatively more distant behind the typhoon center due to faster speed of the typhoon movement (Figure 3a–d), compared with those during 06:00 UTC, 22 October to 06:00 UTC, 23 October (Figure 3e–i).

Figure 6a shows a further quantitative analysis of the relationship between the localization deviations and the typhoon moving speed (calculated from the best-track locations at each 6-h time interval) during its life span. The correlation coefficient between the localization deviations and the typhoon moving speed was about 0.79 after 06:00 UTC, 19 October, suggesting that the localization deviation is typhoon moving speed-dependent.

The detection of the *p*-wave DF microseisms also depends on the array response function (ARF), which is controlled by the deployment of the array, including the aperture, configuration and interstation spacing. Although the beamforming method here is based on travel time difference, the desired signals are mostly teleseismic *p* waves, which would transverse the array with high incident angles. Therefore the plane wave ARF of the NECESSArray as following is applied as an approximation:

$$|A(k - k_0)|^2 = \left| \frac{1}{N} \sum_{n=1}^{N} e^{(2\pi i(k-k_0)\cdot r_n} \right|^2, \quad (4)$$

where k is the wave number vector, k_0 is the reference wave number vector, and r_n the positions of the stations, is shown in Figure 7. The ARF of NECESSArray has a unique main lobe, which is relatively larger in the N–S direction than in the E–W direction. That is because the deployment of the NECESSArray stations was mainly oriented in an approximate E–W direction (Figure 1). As a result, the localization resolution of the *p*-wave DF microseism source regions in the N–S direction was relatively poorer than in the E–W direction, as shown in Figure 3 [35,41]. Here we define the localization resolution with the major axis length of the located source regions corresponding with top 10%, 15% or 20% strongest amplitudes of the beamformer outputs (Figure 6b). When Lupit was moving mainly northward before 06:00 UTC, 19 October, the poor localization resolution in the N–S direction could probably lead to inaccurate localization results, and thus a weak correlation between the localization deviations and the typhoon moving speed at that time (Figure 6a).

The localization deviations might also depend on the directions of the typhoon movement. When a typhoon turns, the ocean wave-wave interactions for the generation of DF microseisms can occur beyond the typhoon track (Figure 5c). For example, Figure 8 shows the located source regions of the *p*-wave DF microseisms generated by Lupit at 18:00 UTC, 24 October and 00:00 UTC, 25 October. The identified source regions were formed by the nonlinear interaction between the ocean waves, which were probably generated before and after the abrupt change of the Lupit course at 00:00 UTC, 23 October, respectively. Therefore, the source regions were mainly located between the two corresponding segments of the Lupit course before and after the abrupt change of the course, rather than along the track, as shown in Figure 8.

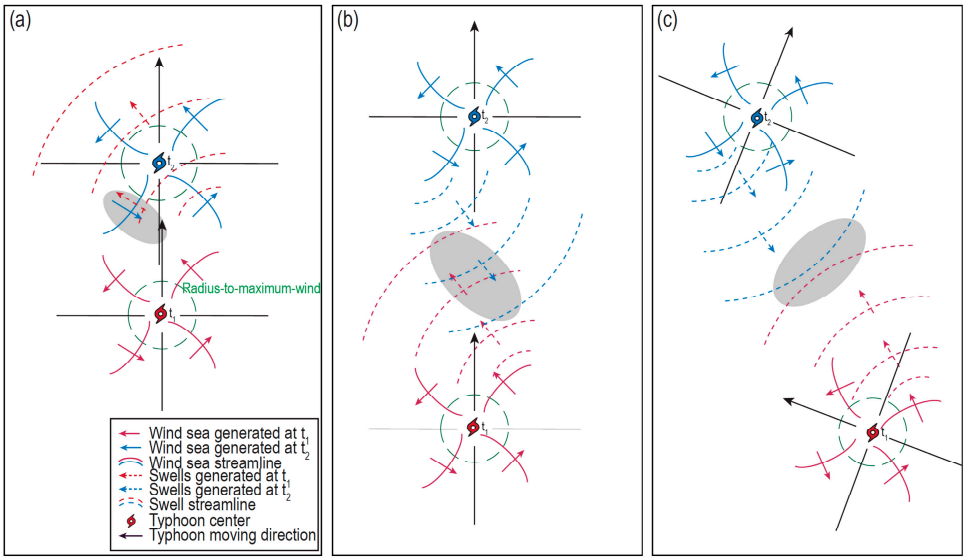

Figure 5. Schemes for the DF microseism source regions under a hypothetical typhoon in the Northern hemisphere. Gray ellipses represent schematically the main source regions of DF microseisms with "wave-wave interaction" when (**a**) typhoon moves northward with relatively slower velocity than the ocean wave propagates; (**b**) typhoon moves northward with relatively faster velocity than the ocean wave propagates; and (**c**) typhoon movement direction changes. Red and blue hurricane symbols indicate the typhoon centers at an earlier time t1 and a later time t2, respectively. Dashed arrows and curved lines show the propagation directions and streamlines of swells generated at different time. Solid arrows and curved lines show the propagation directions and streamlines of the locally generated wind sea at different time. Black arrows indicate the direction of typhoon movement.

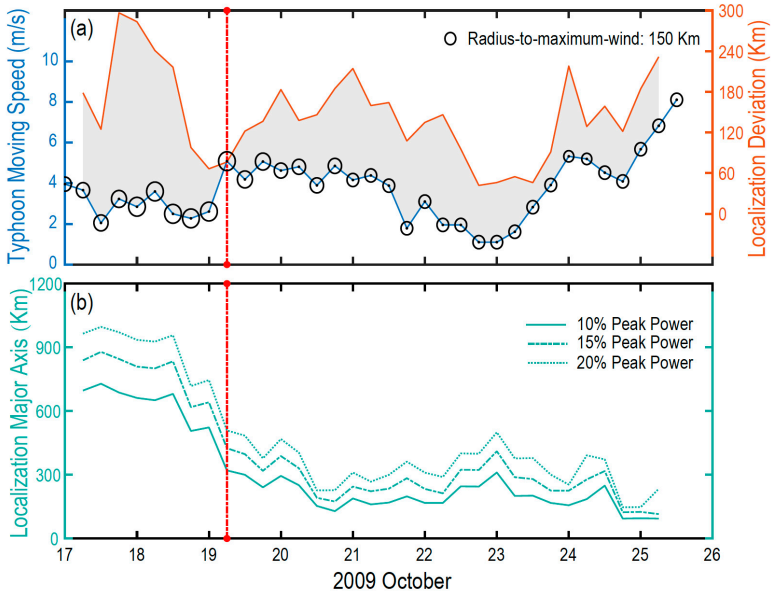

Figure 6. (**a**) Localization deviation (orange solid line, calculated by the distance between the *p*-wave DF microseism source region located by the beamformer outputs and the typhoon center according to the best-track data of RSMC) compared with the typhoon moving speed (blue solid line). The black circles represent the radius-to-maximum-wind. The RMS error of the localization results after 06:00 UTC, 19 October is about 124.2 km. (**b**) Localization resolution measured by the length of the major axis of the located source regions corresponding to the top 10%, 15% and 20% strongest amplitudes of the beamformer outputs.

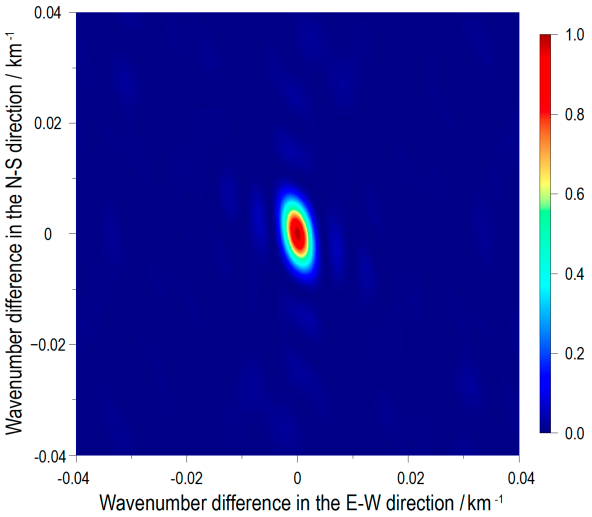

Figure 7. Array response function of NECESSArray with array geometry presented in Figure 1.

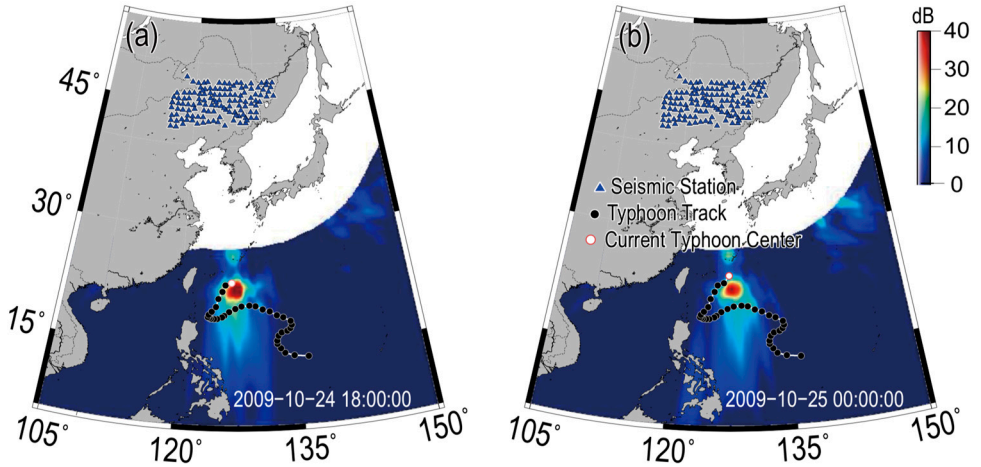

Figure 8. Source locations of Lupit-generated *p*-wave DF microseisms in the form of beamformer outputs using the NECESSArray data at (**a**) 18:00 UTC, 24 October; and (**b**) 00:00 UTC, 25 October. The beams were calculated and stacked over the frequency band of 0.18-0.21 Hz. The solid circles indicate the track of Lupit with the white one representing the current location of typhoon center according to the best-track data of the Regional Specialized Meteorological Center (RSMC).

The localization method could also be affected by the *p*-wave DF microseisms generated in coastal source regions. According to the *Longuet–Higgins* theory [10], DF microseisms are thought to originate from nonlinear interactions between the ocean waves propagating in nearly opposite directions and with almost the same frequencies. The frequency of the DF microseisms is equal to the sum of one of the ocean waves. Such ocean wave-wave interaction could also occur at coastal areas, where incident ocean swells induced by a typhoon are reflected by coastlines after long-distance propagation and then interfere with subsequent incident ocean swells. The coastal source regions of DF microseisms could also provide a strong *p*-wave contribution, and be detected as a *p*-wave peak beam in the beamformer outputs. We investigated the source regions of the *p*-wave DF microseisms generated by Lupit in different frequency bands when Lupit was approaching the Luzon Island. We found that the coastal-generated *p*-wave DF microseisms had a relatively lower dominant frequency band of 0.14–0.16 Hz, compared with the dominant frequency band (~0.18–0.21 Hz) of the *p*-wave DF microseisms generated near typhoon centers (e.g., Figure 9). That is because the dominant frequencies

of the ocean swells incident to the coasts have decreased due to the dispersion effect during the long-distance propagation after being generated by Lupit [42]. Therefore, although the beamformer outputs allow us to locate both the coastal source regions and the source regions near the typhoon center of the *p*-wave DF microseisms, the source regions could be separated in frequency domain while using this beamforming method to track typhoon centers.

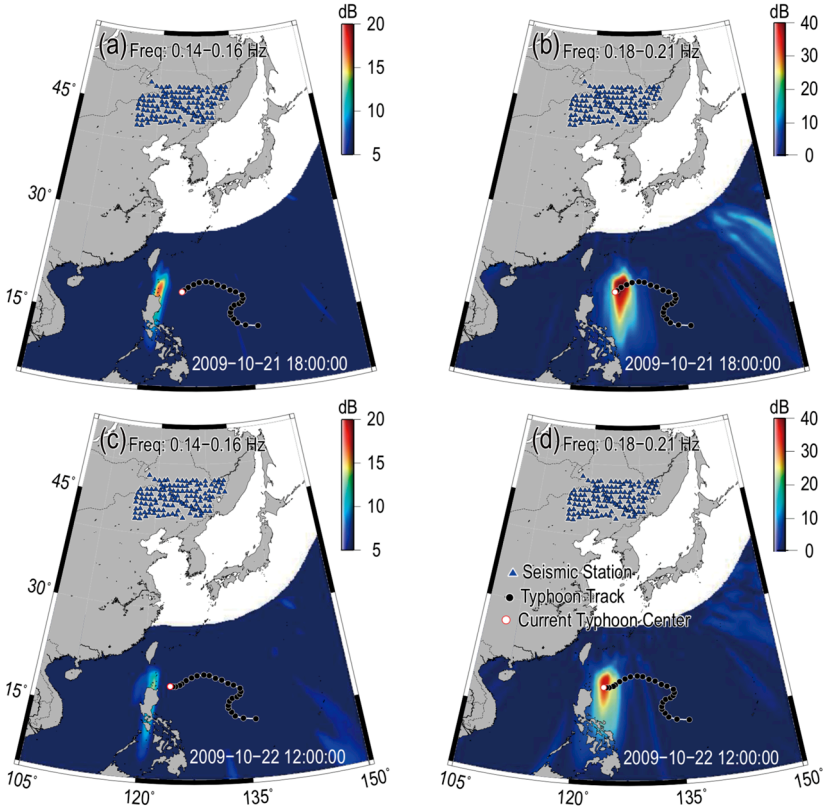

Figure 9. Source locations of Lupit-generated *p*-wave DF microseisms in the frequency band of (**a**,**c**) 0.14–0.16 Hz and (**b**,**d**) 0.18–0.21 Hz in the form of beamformer outputs using the NECESSArray data at 18:00 UTC, 21 October and 12:00 UTC, 22 October 2009. The solid circles indicate the track of Lupit with the white one representing the current location of typhoon center according to the best-track data of RSMC.

5. Conclusions

The *p*-wave DF microseisms generated by typhoon Lupit over the western Pacific Ocean were observed by the seismological array NECESSArray deployed in NE China. Frequency-domain beamforming method has been applied to locate the source regions of the *p*-wave DF microseisms. The located source regions of the *p*-wave DF microseisms in the frequency band of ~0.18–0.21 Hz were basically comparable to the typhoon centers with RMS error around ~120 km, likely associated with the strongest nonlinear interactions of ocean waves near the typhoon center. The *p*-wave DF microseisms generated in coastal source regions were also observed in the beamformer outputs, but with a relatively lower dominant frequency band of ~0.14–0.16 Hz. These observations show that although the localization deviations may depend on both the speed and directions of typhoon movement, the *p*-wave DF microseisms generated near typhoon centers could be used as a proxy to locate and track typhoons over oceans from underwater in a near-real-time and continuous manner.

Supplementary Materials: The following are available online at http://www.mdpi.com/2072-4292/10/2/235/s1, Video S1: Lupit_Bodywave.Freq_0.18_0.21Hz.avi, Video S2: Lupit_Bodywave.Freq_0.14_0.16Hz.avi.

Acknowledgments: NECESSArray waveform data used in this study are openly available from the IRIS Data Management System under experiment code YP 2009–2011. MODIS data are provided by the NASA (National Aeronautics and Space Administration). The manuscript benefited from thoughtful discussion with Renhao Wu. We would like to thank Paul Wessel and Walter H. F. Smith for the use of the Generic Mapping Tools (GMT) software [43]. This work was supported by the Natural Science Foundation of Zhejiang Province (LZ14D060001) and the National Natural Science Foundation of China (grant #41104027, #41374070). The views, opinions, and findings contained in this report are those of the authors and should not be construed as an official NOAA or U.S. Government position, policy or decision.

Author Contributions: Jianmin Lin and Xiaofeng Li came up with the original idea; Jianmin Lin, Weitao Wang, Sunke Fang and Hong Zheng analyzed the data; Yating Wang and Chao Chen collected the data; all authors contributed to the writing and revising of the manuscript.

Conflicts of Interest: The authors declare no conflict of interest.

References

1. Gerstoft, P.; Fehler, M.C.; Sabra, K.G. When Katrina hit California. *Geophys. Res. Lett.* **2006**, *33*, L17308. [CrossRef]
2. Wilson, J.D.; Makris, N.C. Ocean acoustic hurricane classification. *J. Acoust. Soc. Am.* **2006**, *119*, 168–181. [CrossRef] [PubMed]
3. Wilson, J.D.; Makris, N.C. Quantifying hurricane destructive power, wind speed, and air-sea material exchange with natural undersea sound. *Geophys. Res. Lett.* **2008**, *35*, L10603. [CrossRef]
4. Chi, W.C.; Chen, W.J.; Kuo, B.Y.; Dolenc, D. Seismic monitoring of western Pacific typhoons. *Mar. Geophys. Res.* **2010**, *31*, 239–251. [CrossRef]
5. Chan, H.C.; Chen, C.F. Underwater acoustic sensing applied to estimation of typhoon wind speed. *Int. J. Remote Sens.* **2012**, *33*, 7398–7412. [CrossRef]
6. Sun, T.H.Z.; Xue, M.; Le, K.P.; Zhang, Y.W.; Xu, H.P. Signatures of ocean storms on seismic records in South China Sea and East China Sea. *Mar. Geophys. Res.* **2013**, *34*, 431–448. [CrossRef]
7. Sufri, O.; Koper, K.D.; Burlacu, R.; Foy, B.D. Microseisms from Superstorm Sandy. *Earth Planet. Sci. Lett.* **2014**, *402*, 324–336. [CrossRef]
8. Davy, C.; Barruol, G.; Fontaine, F.R.; Sigloch, K.; Stutzmann, E. Tracking major storms from microseismic and hydroacoustic observations on the seafloor. *Geophys. Res. Lett.* **2014**, *41*, 8825–8831. [CrossRef]
9. Zhao, Z.X.; D'Asaro, E.A.; Nystuen, J.A. The sound of tropical cyclones. *J. Phys. Oceanogr.* **2014**, *44*, 2763–2778. [CrossRef]
10. Longuet-Higgins, M.S. A theory of the Origin of Microseisms. *Philos. Trans. R. Soc. Lond. Ser. A Math. Phys. Sci.* **1950**, *243*, 1–35. [CrossRef]
11. Lin, J.M.; Lin, J.; Xu, M. Microseisms generated by super typhoon Megi in the western Pacific Ocean. *J. Geophys. Res. Oceans* **2017**, *122*, 9518–9529. [CrossRef]
12. Friedrich, A.; Kruger, F.; Klinge, K. Ocean generated microseismic noise located with the Grafenberg array. *J. Seismol.* **1998**, *2*, 47–64. [CrossRef]
13. Bromirski, P.D. Vibrations from the "Perfect Storm". *Geochem. Geophy. Geosyst.* **2001**, *2*, 1030. [CrossRef]
14. Gerstoft, P.; Shearer, P.M.; Harmon, N.; Zhang, J. Global P, PP, and PKP wave microseisms observed from distant storms. *Geophys. Res. Lett.* **2008**, *35*, L23306. [CrossRef]
15. Zhang, J.; Gerstoft, P.; Bromirski, P.D. Pelagic and coastal sources of *P*-wave microseisms: Generation under tropical cyclones. *Geophys. Res. Lett.* **2010**, *37*, L15301. [CrossRef]
16. Hasselmann, K.A. Statistical analysis of the generation of microseisms. *Rev. Geophys.* **1963**, *1*, 177–210. [CrossRef]
17. Haubrich, R.A.; McCamy, K. Microseisms: Coastal and pelagic sources. *Rev. Geophys.* **1969**, *7*, 539–571. [CrossRef]
18. Webb, S.C. Broadband seismology and noise under the ocean. *Rev. Geophys.* **1998**, *36*, 105–142. [CrossRef]
19. Ardhuin, F.; Gualtieri, L.; Stutzmann, E. How ocean waves rock the Earth: Two mechanisms explain microseisms with periods 3 to 300 s. *Geophys. Res. Lett.* **2015**, *42*, 765–772. [CrossRef]
20. Ardhuin, F.; Stutzmann, E.; Schimmel, M.; Mangeney, A. Ocean wave sources of seismic noise. *J. Geophys. Res.* **2011**, *116*, C09004. [CrossRef]

21. LaCoss, R.T.; Kelly, E.J.; Toksöz, M.N. Estimation of seismic noise using Arrays. *Geophysics* **1969**, *34*, 21–38. [CrossRef]
22. Cessaro, R. Sources of primary and secondary microseisms. *Bull. Seismol. Soc. Am.* **1994**, *84*, 142–148.
23. Bromirski, P.D.; Duennebier, F.K. The near-coastal microseism spectrum: Spatial and temporal wave climate relationships. *J. Geophys. Res.* **2002**, *107*, ESE 5-1–ESE 5-20. [CrossRef]
24. Tanimoto, T.; Ishimaru, S.; Alvizuri, C. Seasonality in particle motion of microseisms. *Geophys. J. Int.* **2006**, *166*, 253–266. [CrossRef]
25. Tanimoto, T. Excitation of microseisms. *Geophys. Res. Lett.* **2007**, *34*, L05308. [CrossRef]
26. Gerstoft, P.; Tanimoto, T. A year of microseisms in southern California. *Geophys. Res. Lett.* **2007**, *34*, L20304. [CrossRef]
27. Juretzek, C.; Hadziioannou, C. Where do ocean microseisms come from? A study of Love-to-Rayleigh wave ratios. *J. Geophys. Res. Solid Earth* **2016**, *121*, 1–16. [CrossRef]
28. Koper, K.D.; Foy, B.D. Seasonal anisotropy of short-period seismic noise recorded in South Asia. *Bull. Seismol. Soc. Am.* **2008**, *98*, 3033–3045. [CrossRef]
29. Koper, K.D.; Foy, B.D.; Benz, H. Composition and variation of noise recorded at the Yellowknife Seismic Array, 1991–2007. *J. Geophys. Res.* **2009**, *114*, B10310. [CrossRef]
30. Landès, M.; Hubans, F.; Shapiro, N.M.; Paul, A.; Campillo, M. Origin of deep ocean microseisms by using teleseismic body waves. *J. Geophys. Res.* **2010**, *115*, B05302. [CrossRef]
31. Ramirez, J.E. An experimental investigation of the nature and origin of microseisms at St. Louis, Missouri. *Bull. Seismol. Soc. Am.* **1940**, *30*, 35–84.
32. Gilmore, M.H. Microseisms and ocean storms. *Bull. Seismol. Soc. Am.* **1946**, *36*, 89–119.
33. Wilson, J.D. Quantifying Hurricane Wind Speed with Undersea Sound. Ph.D. Dissertation, Joint Program of Massachusetts Institute of Technology and Woods Hole Oceanographic Institution, Cambridge, MA, USA, 14 July 2006.
34. Wang, J.Y.; Li, F.H. Preliminary study on underwater ambient noise generated by typhoons. *Chin. Phys. Lett.* **2015**, *32*, 044301. [CrossRef]
35. Rost, S.; Thomas, C. Array seismology: Methods and applications. *Rev. Geophys.* **2002**, *40*, 1008. [CrossRef]
36. Bensen, G.D.; Ritzwoller, M.H.; Barmin, M.P.; Levshin, A.L.; Lin, F.; Moschetti, M.P.; Shapiro, N.M.; Yang, Y. Processing seismic ambient noise data to obtain reliable broad-band surface wave dispersion measurements. *Geophys. J. Int.* **2007**, *169*, 1239–1260. [CrossRef]
37. Kennett, B.L.N.; Engdahl, E.R.; Buland, R. Constraints on seismic velocities in the Earth from travel times. *Geophys. J. Int.* **1995**, *122*, 108–124. [CrossRef]
38. Zambon, J.; He, R.; Warner, J. Investigation of hurricane Ivan using the coupled ocean-atmosphere-wave-sediment transport (COAWST) model. *Ocean Dyn.* **2014**, *64*, 1535–1554. [CrossRef]
39. Holthuijsen, L.H.; Powell, M.D.; Pietrzak, J.D. Wind and waves in extreme hurricanes. *J. Geophys. Res.* **2012**, *117*, C09003. [CrossRef]
40. Shao, W.Z.; Li, X.F.; Hwang, P.; Zhang, B.; Yang, X.F. Bridging the gap between cyclone wind and wave by C-band SAR measurements. *J. Geophys. Res. Oceans* **2017**, *122*, 6714–6724. [CrossRef]
41. Harjes, H.P.; Henger, M. Array-Seismologie. *Z. Geophs.* **1973**, *39*, 865–905.
42. Cathles, L.M., IV; Okal, E.A.; MacAyeal, D.R. Seismic observations of sea swell on the floating Ross Ice Shelf, Antarctic. *J. Geophys. Res.* **2009**, *114*, F02015. [CrossRef]
43. Wessel, P.; Smith, W.H.F. New improved version of Generic Mapping Tools released. *EOS Trans. AGU* **1998**, *79*, 579. [CrossRef]